

Colossal Band Renormalization and Stoner Ferromagnetism induced by Electron-Antiferromagnetic-Magnon Coupling

T. L. Yu,¹ R. Peng,^{1,2} M. Xu,¹ W. T. Yang,¹ Y. H. Song,¹ C. H. P. Wen,¹ Q.
Yao,¹ X. Lou,¹ T. Zhang,¹ W. Li,¹ X. Y. Wei,¹ J. K. Bao,³ G. H. Cao,³ P.
Dudin,⁴ J. D. Denlinger,⁵ V. N. Strocov,⁶ H. C. Xu,^{1,*} and D. L. Feng^{1,2,7,8,†}

¹*Laboratory of Advanced Materials, State Key Laboratory
of Surface Physics and Department of Physics,
Fudan University, Shanghai 200438, People's Republic of China*

²*Shanghai Research Center for Quantum Sciences,
Shanghai 201315, People's Republic of China*

³*Department of Physics, Zhejiang University,
Hangzhou 310027, People's Republic of China*

⁴*Diamond Light Source, Harwell Science and Innovation
Campus, Didcot OX11 0DE, United Kingdom*

⁵*Advanced Light Source, 1 Cyclotron Road Lawrence
Berkeley National Laboratory Berkeley, CA 94720-8229, USA*

⁶*Swiss Light Source, Paul Scherrer Institut, CH-5232 Villigen PSI, Switzerland*

⁷*Collaborative Innovation Center of Advanced Microstructures, Nanjing 210093, China*

⁸*Hefei National Laboratory for Physical Science at Microscale,
CAS Center for Excellence in Quantum Information and Quantum Physics,
and Department of Physics, University of Science and Technology of China, Hefei 230026*

Abstract

The interactions between electrons and antiferromagnetic magnons (AFMMs) are important for a large class of correlated materials. For example, they are the most plausible pairing glues in high-temperature superconductors, such as cuprates and iron pnictides. However, unlike electron-phonon interactions (EPIs), clear-cut observations regarding how electron-AFMM interactions (EAIs) affect the band structure are still lacking. Consequently, critical information on the EAIs, such as its strength and doping dependence, remains elusive. Here we directly observe that EAIs induces a kink structure in the band dispersion in $\text{Ba}_{1-x}\text{K}_x\text{Mn}_2\text{As}_2$, and subsequently unveil several key characteristics of EAIs. We found that the coupling constant of EAIs can be as large as 6, and it shows huge doping dependence and temperature dependence, all in stark contrast to the behaviors of EPI and beyond our current understanding of EAIs. Such a colossal renormalization of electronic bands by EAIs drives the system to the Stoner criteria, giving the intriguing ferromagnetic state in $\text{Ba}_{1-x}\text{K}_x\text{Mn}_2\text{As}_2$. Our results expand the current knowledge of EAIs, which may facilitate the further understanding of many correlated materials where EAIs play a critical role, such as high-temperature superconductors.

*Electronic address: xuhaichao@fudan.edu.cn

†Electronic address: dlfeng@fudan.edu.cn

Electron-boson interactions belong to the most fundamental microscopic processes in solids, which are responsible for various fascinating properties. For example, electron-phonon interactions (EPIs) could result in conventional superconductivity or charge density waves [1, 2], whereas the high temperature superconductivity in cuprate and iron-based superconductors is proposed to be related to the interactions between electrons and antiferromagnetic (AFM) spin fluctuations, *i.e.*, magnons [3–5]. The electron-boson interactions “dress” the electrons up, and convert the electrons into quasiparticles. Consequently, the band structure is renormalized, and sometimes an abrupt distortion in the otherwise smooth band dispersion can be detected by angle resolved photoemission spectroscopy (ARPES) [6, 7]. More specifically, a kink structure has been widely observed in the dispersion along the nodal direction of many cuprate superconductors [8–12], which is now attributed to the EPI as it is present in the heavily overdoped regime without many AFM fluctuations [13–16]. Theoretically, the effects of electron-boson interaction can be described by a complex self-energy of the electronic structure [6, 7]. Based on the ARPES data, one can extract the self-energy and the Eliashberg function determined by both the electron-boson matrix element g (*i.e.* interaction potential) and the material-specific bosonic structure [17]. Meanwhile, the electron-boson coupling constant λ , which characterizes the total renormalization strength and directly gives T_c in BCS theory, is found to be less than 1 for electron-phonon interaction in most metals [13, 14, 18].

The magnon effects on the electronic degrees of freedom have been hard to detect in general, either ferromagnetic or antiferromagnetic. In ferromagnets, slight deviations from parabolic dispersion are suspected to be from ferromagnetic magnons but embedded in the electron-electron correlation effect [19–21], while a kink well above magnon energy is dominated by the Stoner excitations rather than magnons [22]. For AFMM, its contribution to the electronic self-energy has not been experimentally identified, although electron-AFMM interactions (EAIs) holds the key to the general understanding of many correlated phenomena like unconventional superconductivity. The energy scale of AFM spin fluctuations is comparable to the bandwidth in cuprates or iron pnictides, which would lead to a renormalization of the entire band rather than a kink near the Fermi energy (E_F). Therefore, one cannot isolate or identify the EAIs in the retrieved total self-energy.

To reveal the characteristics of the EAIs, one requires a compound that has weak electron correlations and robust AFMM excitations. This dilemma condition is usually difficult to fulfil, but could be realized in $\text{Ba}_{1-x}\text{K}_x\text{Mn}_2\text{As}_2$. BaMn_2As_2 is an isostructure material for 122-type Fe-

based superconductors [23]. It is an AFM insulator (AFI) with a Néel temperature $T_N = 625$ K. The magnetic moments of Mn^{2+} ions in BaMn_2As_2 point along the c axis, forming a G-type AFM order (Fig. 1b). K doping turns $\text{Ba}_{1-x}\text{K}_x\text{Mn}_2\text{As}_2$ into a metal. Despite of the carrier doping, the T_N is slightly suppressed and large magnetic moments persist (Fig. 1a) (ref. 24, 25). Inelastic neutron scattering studies find strong AFMM excitations across the phase diagram [26]. The electron-electron correlations are weak according to previous studies on BaMn_2As_2 (ref. 27). At $x > 0.19$, it shows a novel ferromagnetic ground state (FM) with the FM moments in the ab -plane contributed by As-4*p* orbital rather than the canting of Mn AFM moments [25, 28], while the underlying mechanism of the emergent itinerant FM is unknown. If the weak electron-electron correlations remains in $\text{Ba}_{1-x}\text{K}_x\text{Mn}_2\text{As}_2$ following the parent compound BaMn_2As_2 [27], it would be an ideal playground for studying EAIs, as its AFMM excitations should be strong.

Weak electron correlations in $\text{Ba}_{1-x}\text{K}_x\text{Mn}_2\text{As}_2$

Figures 1d-f show ARPES results measured using vacuum ultra-violet (VUV) photons, which resolve the Fermi surface structure of $\text{Ba}_{1-x}\text{K}_x\text{Mn}_2\text{As}_2$ ($x = 0.3$) in its three-dimensional Brillouin zone. In the Γ -X-M plane measured with 78 eV photons, the Fermi surfaces consist of a large pocket α and two small elliptical pockets β and β' perpendicular to each other, all centred at Γ . The α band is absent in the ZRA plane and highly dispersive along k_z , forming a drum-shaped Fermi surface in the $k_y - k_z$ plane. β and β' are two-dimensional with negligible dispersion along k_z . Except for some variation in the spectral weight due to the photoemission matrix element, the Fermi surfaces measured using VUV photons are consistent with the soft X-ray ARPES results (Supplementary Section 1), confirming the bulk nature of the measured bands. The single set of bands and Fermi surface, and the fact that the Fermi surface volume is consistent with its doping level demonstrate that $\text{Ba}_{1-x}\text{K}_x\text{Mn}_2\text{As}_2$ samples are homogeneous (Supplementary Section 2, [27, 30, 32]).

Along Γ -X, the bands α , β , and β' that cross E_F are all resolved, showing hole-like dispersions (Figs. 1g-i). Both the Fermi surface structure and band dispersion of $\text{Ba}_{1-x}\text{K}_x\text{Mn}_2\text{As}_2$ roughly agree with a rigid band shift of the pristine BaMn_2As_2 [24, 27]. The overall bandwidths near E_F show little renormalization compared with the DFT calculations of BaMn_2As_2 (ref. 25, 27), consistent with the weakly correlated As-4*p* states. The weak band renormalization in $\text{Ba}_{1-x}\text{K}_x\text{Mn}_2\text{As}_2$ is distinct from the strongly renormalized bands in the isostructural $\text{Ba}_{1-x}\text{K}_x\text{Fe}_2\text{As}_2$ (ref. 33). The

weak electron-electron correlation would contribute little electronic self-energy near E_F , which provides a clean playground for studying electron-boson interactions in $\text{Ba}_{1-x}\text{K}_x\text{Mn}_2\text{As}_2$.

Strong electron-magnon interactions in $\text{Ba}_{1-x}\text{K}_x\text{Mn}_2\text{As}_2$

Band α shows a kink around the binding energy $E_B=50$ meV, which is better visualized in the second derivative image and MDCs (Figs. 2a-b). This kink in electronic dispersion is a general signature of electron-boson interactions [7]. The Fermi velocity v_F is reduced from the bare band velocity v_F^0 by a factor of ~ 7 (Fig. 2a), from which one can estimate the electron-boson coupling

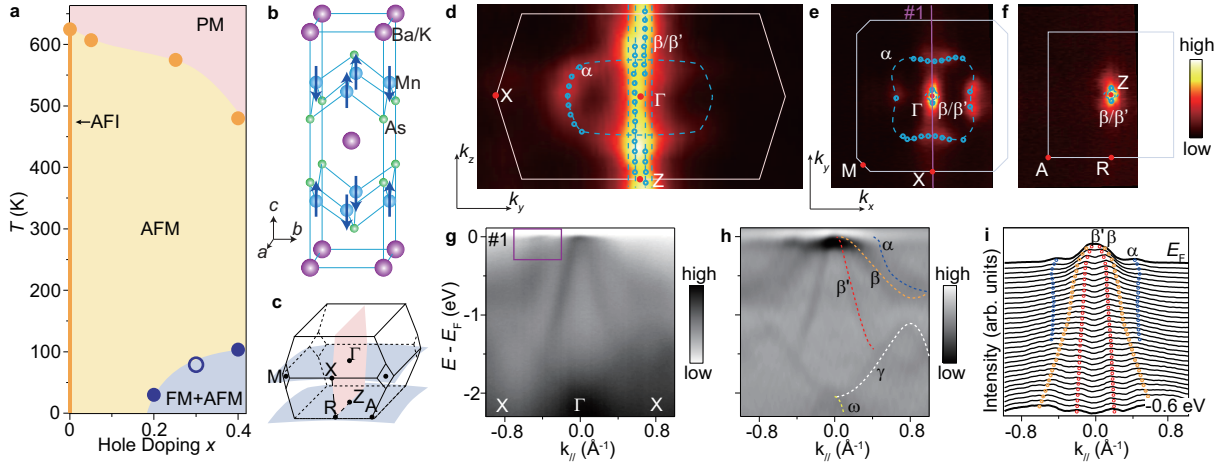


FIG. 1: Phase diagram and the basic electronic structure of $\text{Ba}_{1-x}\text{K}_x\text{Mn}_2\text{As}_2$ ($x = 0.3$). (a) Phase diagram of $\text{Ba}_{1-x}\text{K}_x\text{Mn}_2\text{As}_2$. The open circle indicates the Curie temperature determined by magnetic susceptibility measurements on our sample. The filled circles indicate data from ref. 25, 29–31. (b-c) Crystal structure of $\text{Ba}_{1-x}\text{K}_x\text{Mn}_2\text{As}_2$ and the corresponding three-dimensional Brillouin zone. The blue arrows indicate the alignment of the Mn magnetic moments in the G-type antiferromagnetic (AFM) state. (d-f) Photoemission intensity maps in the high symmetric planes of the Brillouin zone, integrated over an energy window of $E_F \pm 20$ meV. The k_y-k_z map in the ΓXZ plane is measured with photon energies ranging from 58 eV to 100 eV, while the k_x-k_y maps in the ΓXM plane and ZRA plane are measured with 78 eV and 62 eV photons, respectively. (g-h) Photoemission intensity and its second derivative with respect to energy along cut #1 in panel e. The bands are outlined by the dashed curves. (i) Momentum distribution curves (MDCs) along cut #1. The circles track the local maxima for the dispersion of bands α , β and β' . The ARPES data were measured at 30 K.

constant $\lambda=v_F^0/v_F-1$ to be as large as 6. The observed electron-boson coupling constant is colossal as compared to those relating with electron ferromagnetic magnons interactions and EPI (Fig. 2c) [18, 20, 21, 34–41]

Based on the quasiparticle spectra measured by ARPES, we can extract the complex self-energy. The real part of the self-energy is obtained by $\text{Re } \Sigma(E) = [k(E) - k_0(E)] \times |v_F^0|$, where $k_0(E)$ is the bare band momentum and v_F^0 is the bare band velocity. The imaginary part of the self-energy can be obtained by $|\text{Im } \Sigma(E)| = |v_F^0| \times \text{FWHM}/2$, where FWHM is the full-width at half-maximum of the MDC peaks. By analyzing the kink of $\text{Ba}_{1-x}\text{K}_x\text{Mn}_2\text{As}_2$, the real part of the self-energy $\text{Re } \Sigma$ peaks at approximately 50 meV (Fig. 2d), where the imaginary part of the self-energy $\text{Im } \Sigma$ also shows a step (Fig. 2e), indicating the energy scale of the corresponding bosonic modes. The Kramers-Kronig (KK) transform of $\text{Im } \Sigma$ matches well with $\text{Re } \Sigma$ below 100 meV (Fig. 2d), while that of $\text{Re } \Sigma$ also matches $\text{Im } \Sigma$ well after including a constant background and a quadratic term (Fig. 2e). The quadratic term from the electron-electron scattering accounts for the deviation above 100 meV. The KK conjugation of $\text{Im } \Sigma$ and $\text{Re } \Sigma$ demonstrates the self-consistency of the self-energy extraction.

The obtained $\text{Im } \Sigma$ and $\text{Re } \Sigma$ consistently indicate a bosonic energy scale that extends from 0 meV to 120 meV and peaks at approximately 50 meV (Figs. 2d-e). Given the quasiparticle self-energy, we can estimate the Eliashberg function $\alpha^2F(\omega)$ of the kink by $\alpha^2F(\omega) = \frac{\partial \text{Im} \Sigma(E)}{\pi \partial E} \Big|_{E=\omega}$ [see Methods], which characterizes the corresponding bosonic density of states weighted by their effective interactions with electrons [7]. As shown in Fig. 2f, the energy scale of $\alpha^2F(\omega)$ is distinct from the phonon energies below 25 meV according to the inelastic neutron scattering (INS) on $\text{Ba}_{1-x}\text{K}_x\text{Mn}_2\text{As}_2$ ($x = 0.25$) (ref. 26), and the phonon spectra calculated for $\text{Ba}_{1-x}\text{K}_x\text{Mn}_2\text{As}_2$ ($x = 0$ and 0.5) (Supplementary Section 3, [42–45]), which excludes the phonons as the origin of the kink. Finite effect on the electronic self-energy from EPI could exist below 25 meV, but its observation is hindered by the much larger contribution from the electron boson interaction that peaks at approximately 50 meV. Instead, the energy scale of $\alpha^2F(\omega)$ matches that of magnon spectra of $\text{Ba}_{0.75}\text{K}_{0.25}\text{Mn}_2\text{As}_2$ (Fig. 2f), which has been resolved by the INS magnetic intensity and well reproduced by Heisenberg-model-based simulations (Supplementary Section 4, [26, 46]). After considering the momentum restriction of single magnon absorption/emission processes, the simulated $\alpha^2F(\omega)$ also exhibits the same energy scale (Supplementary Section 5, [26]). The consistent energy scale provides compelling evidence that the kink feature in $\text{Ba}_{1-x}\text{K}_x\text{Mn}_2\text{As}_2$ is due to the strong interactions between itinerant electrons and a large range of AFMMs allowed by the energy

and momentum restrictions of the corresponding scattering processes.

Figures 3a-f show that kinks are present for various dopings, indicating the robust presence of electron-boson interactions in $\text{Ba}_{1-x}\text{K}_x\text{Mn}_2\text{As}_2$. Following the same procedure, $\alpha^2F(\omega)$ is obtained for each doping. The intensity gradually shifts towards lower energy with increasing doping (Fig. 3g), which is consistent with the doping dependent energy shift of magnons as revealed by both the INS magnetic intensity and the calculated magnon DOS (Supplementary Section 4, [26, 46]). The intensity of $\alpha^2F(\omega)$ increases by nearly 50% from $x = 0.1$ to $x = 0.2$, and is similar between $x = 0.2$ and 0.3 , indicating a nonlinear doping dependence of the EAIs coupling constant. As the doping increases from $x = 0.1$ to 0.3 , the bare band velocity v_F^0 increases from $\sim 3.9 \text{ eV}\cdot\text{\AA}$ to $\sim 7.7 \text{ eV}\cdot\text{\AA}$, while the renormalized Fermi velocity v_F remains at approximately $\sim 1.1 \text{ eV}\cdot\text{\AA}$ (Figs. 3a-c). Therefore, the EAIs constant $\lambda=v_F^0/v_F-1$ increases with higher doping (Fig. 3h), as the system enters deep into the ferromagnetic regime.

The mechanism of the ferromagnetic ground state

The microscopic origin of the weak ferromagnetism in $\text{Ba}_{1-x}\text{K}_x\text{Mn}_2\text{As}_2$ has been under debate. The picture of the canted Mn^{2+} local moment [47] was excluded by various studies, and meanwhile, the ferromagnetism was attributed to the spin polarization of As-4*p* holes, suggesting an itinerant picture following Stoner mechanism [28, 31]. Currently, one strong criticism for the Stoner mechanism is that the calculated DOS at E_F ($N(E_F)$) in $\text{Ba}_{1-x}\text{K}_x\text{Mn}_2\text{As}_2$ is too small to meet the Stoner criterion even at the high doping level of $x = 0.4$ (ref. 47). However, the EAIs were not considered in previous calculations, and the observed colossal EAIs would greatly enhance the DOS at E_F . Particularly, it becomes even stronger when entering the ferromagnetic state with increasing doping (Fig. 3h). Therefore, the Stoner mechanism needs to be reexamined.

In addition to increasing the doping level, another route into the ferromagnetic state is through cooling. Figure 4 examines how the electronic structure of $\text{Ba}_{0.7}\text{K}_{0.3}\text{Mn}_2\text{As}_2$ evolves across the Curie temperature. Figure 4a shows that the kink is always present from 30 K to 120 K, indicating that the EAIs persist in both the coexisting FM-AFM phase and the pure AFM phase, however, the Fermi velocity v_F increases from $\sim 0.55 \text{ eV}\cdot\text{\AA}$ to $\sim 0.76 \text{ eV}\cdot\text{\AA}$. As the bare band velocity v_F^0 is almost fixed around $3.8 \text{ eV}\cdot\text{\AA}$, the EAIs coupling constant shows a prominent increase of approximately 50% from 120 K to 30 K (Fig. 4e), and also confirmed by the self-energy analysis (Supplementary Section 6). Meanwhile, as the temperature decreases, a quasiparticle peak

emerges near E_F for both α and β bands (Figs. 4c-d). It becomes sharper at lower temperature due to enhanced coherence in the ferromagnetic phase [48–50]. We characterize the emergence of the quasiparticle peak by its spectral weight, which increases continuously with decreasing temperature. The major enhancement taking place between 90 K and 60 K (Figs. 4f-g), where the broad ferromagnetic transition occurs (Supplementary Section 7). The temperature dependence of the spectral weight follows that of λ , indicating the intimate relationship between the ferromagnetic state and the EAI.

The EAIs in $\text{Ba}_{1-x}\text{K}_x\text{Mn}_2\text{As}_2$ could influence the ferromagnetic state through the DOS at E_F , $N(E_F)$. Considering no EAIs, the bare band DOS $N^0(E_F)$ is approximately $0.2 \text{ spin}^{-1}\text{eV}^{-1}\text{As}^{-1}$ calculated from the measured Fermi surface and bare band velocity [see methods], which is comparable to that estimated by DFT calculations and does not meet the Stoner criteria [47]. After considering the EAIs, $N(E_F)$ is greatly enhanced from $N^0(E_F)$, following the doping dependence and temperature dependence of EAIs coupling constant λ (Fig. 5). $N(E_F)$ becomes most enhanced in the ferromagnetic regime, reaching $1.53 \pm 0.36 \text{ spin}^{-1}\text{eV}^{-1}\text{As}^{-1}$ at $x = 0.3$, which is 3 times of that estimated by DFT calculations at an even higher doping $x = 0.4$ (ref. 47). Clearly, when $N(E_F)$ is roughly above $\sim 1.2 \text{ spin}^{-1}\text{eV}^{-1}\text{As}^{-1}$, $\text{Ba}_{1-x}\text{K}_x\text{Mn}_2\text{As}_2$ enters the ferromagnetic phase. If this corresponds to the Stoner criteria, $I_{\text{As}}N(E_F) \geq 1$, the Stoner parameter of As, I_{As} , is estimated to be approximately 0.8 eV for $\text{Ba}_{0.7}\text{K}_{0.3}\text{Mn}_2\text{As}_2$ with a Curie temperature T_C of 90 K. We note that the Stoner picture based on mean field theory usually fails to predict the T_C of transition-metal ferromagnets with strong local exchange splitting above T_C (ref. 51), however, a crude estimation of T_C by the Stoner criteria could still be feasible on low- T_C weak ferromagnets [52], as $\text{Ba}_{1-x}\text{K}_x\text{Mn}_2\text{As}_2$ is supposed to be. Consistently at 30 K, with this $I_{\text{As}} \sim 0.8 \text{ eV}$, the Stoner criteria are fulfilled just at doping $x = 0.2$, whose T_C is approximately 30 K, while not fulfilled for the doping $x = 0.1$ with no ferromagnetic ground state. These results show that the Stoner mechanism is at work and that the ferromagnetic ground state is driven by the As-4*p* holes renormalized by EAIs.

In a Stoner ferromagnet, exchange band splitting will occur. Considering the finite resolution, the upper limit of exchange splitting is estimated by fitting the MDC peaks of band α with two Lorentzian peaks, which gives a momentum splitting of 0.065 \AA^{-1} in $\text{Ba}_{1-x}\text{K}_x\text{Mn}_2\text{As}_2$ ($x = 0.3$) at 30 K (Supplementary Section 8). Assuming an isotropic splitting over the Fermi surface, this splitting corresponds to a spin polarization of 0.07 holes/f.u. (f.u. = formula unit), which accounts for only 32% of the ferromagnetic moment of $0.25 \mu_B/\text{f.u.}$ at 30 K by magnetic susceptibility mea-

measurements (Supplementary Section 7). Despite that Stoner picture is still at work in driving the ferromagnetism, at least 68% of the ferromagnetic moments are not from itinerant carriers. Since the magnetic moment is found to be of As character based on previous X-ray dichroism measurements [28], our results imply that the non-magnetic element As gives a considerable contribution of local moments. Magnetic moments on non-magnetic atoms could be induced by local environments as exemplified by the V moments observed in VAu₄ (ref. 53, 54). In Ba_{1-x}K_xMn₂As₂, projection of the As-4*p* orbital was found both at the dispersive bands (α , β , and β'), and at the flat bands at higher binding energies with localized nature [27]. Driven by the spontaneous spin polarization of the itinerant As-4*p* holes, the As-4*p* states with both itinerant and localized nature in Ba_{1-x}K_xMn₂As₂ can host an emergent ferromagnetic state with mixed itinerant and localized As moments.

Summary and Outlook

The EAI is one of the fundamental interactions in condensed matter. Our findings illustrate quantitatively how the EAIs can renormalize the electronic band, invoke the Stoner mechanism, and induce ferromagnetism in Ba_{1-x}K_xMn₂As₂. It offers an unprecedented opportunity to directly study the self-energy and Eliashberg function $\alpha^2F(\omega)$ of EAIs, and our quantitative analysis reveals various important facts about the EAIs for the first time.

1. The coupling constant λ of EAIs in Ba_{1-x}K_xMn₂As₂ is as high as 6, which is much higher than any other known electron-boson coupling in metals. High density of states (DOS) of magnons are expected in the Mn AFM order with spin $S=5/2$, which could be partly responsible for the large coupling constant λ . The large coupling constant demonstrates that the effect of the EAIs can be overwhelmingly strong and could dominate the ground states.
2. The EAIs vary strongly with both temperature and doping, even if the AFM order is robust. In the case of in Ba_{1-x}K_xMn₂As₂, the EAIs is enhanced by nearly 150% from $x = 0.1$ to 0.3, which could be induced by the expanded Fermi surface volume and the increased scattering phase space at higher dopings. This observation is in contrast to the EPI, which usually exhibits an opposite behavior.

Our data put constrains on the theories of EAIs. The extracted electronic self-energy and Eliashberg function $\alpha^2F(\omega)$ will motivate future inelastic neutron scattering studies to obtain the magnon

spectra with absolute value, so that the electron-magnon matrix element g and other microscopic characteristics of EAs could be further revealed at a more quantitative level. As these characteristics of the EAs could be general in other materials with AFM excitations, such as high temperature superconductivity in cuprates and iron pnictides, our results would facilitate further understanding of the related emergent phenomena.

Methods

1. Sample growth and characterization.

The $\text{Ba}_{1-x}\text{K}_x\text{Mn}_2\text{As}_2$ single crystals used in this study were grown by the flux method as described elsewhere [25, 55]. The chemical composition and K doping level were determined by electron probe microanalysis (EPMA). The carrier concentrations calculated from Fermi surface volumes based on Luttinger theorem agree well with the chemical doping determined by EPMA measurements, indicating that the $\text{Ba}_{1-x}\text{K}_x\text{Mn}_2\text{As}_2$ sample is of single phase with homogeneous doping level. This is further supported by STM and EPMA measurements over the cleaved surface (Supplementary Section 2, [27, 30, 32]). The magnetic susceptibility was measured by Quantum Design Dynalcoo system (Supplementary Section 7).

2. ARPES experiments.

VUV-ARPES experiments were performed at beamlines BL5-2 of the Stanford Synchrotron Radiation Light Source (SSRL), I05 of the Diamond Light Source, and BL4.0.3 of the Advanced Light Source (ALS). The energy and angular resolutions were set at 15 meV and 0.3° , respectively. SX-ARPES experiments were performed at ADDRESS of the Swiss Light Source [56]. The energy and angular resolutions were set at 80 meV and 0.1° , respectively. All samples were cleaved *in situ* under a vacuum better than 2×10^{-10} mbar and measured under a vacuum better than 8×10^{-11} mbar.

3. Extraction of self-energy and calculation of the coupling constant.

The real part of the self-energy can be obtained by $\text{Re } \Sigma(E, k) = E(k) - \epsilon(k) = (k(E) - k_0(E)) \times |v_F^0|$, where the $\epsilon(k)$, $E(k)$, $k_0(E)$, and v_F^0 are the bare band energy, renormalized energy, bare band

momentum, and bare band velocity, respectively. The bare band is estimated by cubic spline interpolation. The imaginary part of the self-energy can be derived by $|Im\Sigma(E, k)| = |v_F^0| \times (FWHM) / 2$, where $(FWHM)$ is the full-width at half-maximum of the MDC peak and v_F^0 is the bare band velocity. The $Re \Sigma$ and $Im \Sigma$ should be the Kramers-Kronig conjugation of each other before the cut-off energy $E_{max}=115$ meV:

$$Re\Sigma(E, k) = \frac{1}{\pi} \int_{-\infty}^{+\infty} \frac{Im\Sigma(E', k)}{E' - E} dE' \quad E \leq E_{max}$$

$$Im\Sigma(E, k) = \begin{cases} -\frac{1}{\pi} \int_{-\infty}^{+\infty} \frac{Re\Sigma(E', k)}{E' - E} dE' & E \leq E_{max} \\ -\frac{1}{\pi} \int_{-\infty}^{+\infty} \frac{Re\Sigma(E_{max}, k)}{E' - E_{max}} dE' & E > E_{max} \end{cases}$$

The cut-off energy E_{max} is determined by the maximum energy of AFM magnons $\omega_{max} \sim 115$ meV in $Ba_{1-x}K_xMn_2As_2$, above which the electron-electron correlation starts to substantially contribute to the increase in $Im \Sigma$.

The coupling constant is calculated by either the renormalization of the Fermi velocity, or by the Eliashberg function from the self-energy. For both cases, we employ the formula at the $T \rightarrow 0$ limit because the experimental temperatures are far below the T_N of $Ba_{1-x}K_xMn_2As_2$. In the quasielastic approximation where the electronic energy E is much larger than the boson energy ω , the quasiparticle self-energy is determined by the Eliashberg function as [7]:

$$Im\Sigma(E, k; T) = \pi \int_0^{\omega_{max}} \alpha^2 F(E, k; \omega) [1 - f(E - \omega) + f(E + \omega) + 2n(\omega)] d\omega$$

Assuming the $T \rightarrow 0$ limit with $n(\omega) \rightarrow 0$, we have:

$$Im\Sigma(E, k) = \pi \int_0^{\omega_{max}} \alpha^2 F(E, k; \omega) f(E + \omega) d\omega$$

As the electronic energy scale of band α is much larger than the magnon energy scale, the dependence of $\alpha^2 F(E, k; \omega)$ on the electronic energy can be ignored. In this case, the variation in $Im\Sigma(E)$ with E mainly comes from the change in the effective integration range due to the Fermi-Dirac function $f(E + \omega)$. Thus we can estimate $\alpha^2 F(\omega)$ by taking the derivative of $Im\Sigma(E)$:

$$\alpha^2 F(\omega) = \frac{\partial Im\Sigma(E)}{\pi \partial E} \Big|_{E=\omega}$$

To avoid nonphysical values, we set the noise induced negative data points of $\alpha^2 F(\omega)$ to zero. The coupling constant λ can be estimated by:

$$\lambda = 2 \int_0^{\omega_{max}} \frac{\alpha^2 F(\omega)}{\omega} d\omega$$

4. Estimation of density of states $N(E_F)$ and bare-band density of states $N^0(E_F)$

The DOS at E_F , $N(E_F)$, is estimated by the following equations based on its definition:

$$g_n(E) = \int_{S_n(E)} \frac{dS}{4\pi^3} \frac{1}{|\nabla E_n(k)|} \approx \frac{S_{FS}}{4\pi^3} \overline{|v_F^{-1}|}$$

$$N(0) = \frac{1}{2} \times \frac{V_0}{2} g_n \approx \frac{V_0 S_{FS}}{4\pi^3} \overline{|v_F^{-1}|}$$

where V_0 is the volume of the unit cell, S_{FS} is the Fermi surface area and v_F is the Fermi velocity. The bare-band density of states $N^0(E_F)$ are obtained in the same way by replacing the Fermi velocity v_F with the bare-band velocity v_F^0 .

We estimate the S_{FS} of the drum-shaped Fermi pocket α by an analogue of the body-centred tetragonal Brillouin zone, and the S_{FS} of band β/β' based on elliptical cylinders. The uncertainty of the S_{FS} is estimated to be 15%. The $\overline{|v_F^{-1}|}$ calculation is based on the measured value of v_F and an assumed linear change. Thus,

$$\overline{|v_F^{-1}|} = \frac{\int_{v_{Fmin}}^{v_{Fmax}} v_F^{-1} dv_F}{v_{Fmax} - v_{Fmin}} = \frac{\ln(v_{Fmax}) - \ln(v_{Fmin})}{v_{Fmax} - v_{Fmin}}.$$

-
- [1] Bardeen, J., Cooper, L. N. & Schrieffer, J. R. Theory of superconductivity. *Phys. Rev.* **108**, 1175–1204 (1957). URL <https://link.aps.org/doi/10.1103/PhysRev.108.1175>.
- [2] Valla, T. *et al.* Quasiparticle spectra, charge-density waves, superconductivity, and electron-phonon coupling in 2H–NbS₂. *Phys. Rev. Lett.* **92**, 086401 (2004). URL <https://link.aps.org/doi/10.1103/PhysRevLett.92.086401>.
- [3] Scalapino, D. J. The cuprate pairing mechanism. *Science* **284**, 1282–1283 (1999). URL <https://science.sciencemag.org/content/284/5418/1282>. <https://science.sciencemag.org/content/284/5418/1282>.

- [4] Anderson, P. W. *et al.* The physics behind high-temperature superconducting cuprates: the plain vanilla version of RVB. *Journal of Physics: Condensed Matter* **16**, R755–R769 (2004). URL <https://doi.org/10.1088/0953-8984/16/24/r02>.
- [5] Hu, J. Identifying the genes of unconventional high temperature superconductors. *Science Bulletin* **61**, 561–569 (2016). URL <https://doi.org/10.1007/s11434-016-1037-7>.
- [6] Hellsing, B., Eiguren, A. & Chulkov, E. V. Electron-phonon coupling at metal surfaces. *Journal of Physics: Condensed Matter* **14**, 5959–5977 (2002). URL <https://doi.org/10.1088/0953-8984/14/24/2F306>. Publisher: IOP Publishing.
- [7] Hofmann, P., Sklyadneva, I. Y., Rienks, E. D. L. & Chulkov, E. V. Electron-phonon coupling at surfaces and interfaces. *New Journal of Physics* **11**, 125005 (2009). URL [doi:10.1088/1367-2630/11/12/125005](https://doi.org/10.1088/1367-2630/11/12/125005).
- [8] Zhou, X. J. *et al.* Universal nodal fermi velocity. *Nature* **423**, 398–398 (2003). URL <https://doi.org/10.1038/423398a>.
- [9] Johnson, P. D. *et al.* Doping and temperature dependence of the mass enhancement observed in the cuprate $\text{Bi}_2\text{Sr}_2\text{CaCu}_2\text{O}_{8+\delta}$. *Phys. Rev. Lett.* **87**, 177007 (2001). URL <https://link.aps.org/doi/10.1103/PhysRevLett.87.177007>.
- [10] Lanzara, A. *et al.* Evidence for ubiquitous strong electron-phonon coupling in high-temperature superconductors. *Nature* **412**, 510–514 (2001). URL <https://doi.org/10.1038/35087518>.
- [11] Sato, T. *et al.* Observation of band renormalization effects in hole-doped high- T_c superconductors. *Phys. Rev. Lett.* **91**, 157003 (2003). URL <https://link.aps.org/doi/10.1103/PhysRevLett.91.157003>.
- [12] Borisenko, S. V. *et al.* Kinks, nodal bilayer splitting, and interband scattering in $\text{YBa}_2\text{Cu}_3\text{O}_{6+x}$. *Phys. Rev. Lett.* **96**, 117004 (2006). URL <https://link.aps.org/doi/10.1103/PhysRevLett.96.117004>.
- [13] Devereaux, T. P., Cuk, T., Shen, Z.-X. & Nagaosa, N. Anisotropic electron-phonon interaction in the cuprates. *Phys. Rev. Lett.* **93**, 117004 (2004). URL <https://link.aps.org/doi/10.1103/PhysRevLett.93.117004>.
- [14] Ruiz, H. S. & Badía-Majós, A. Nature of the nodal kink in angle-resolved photoemission spectra of cuprate superconductors. *Phys. Rev. B* **79**, 054528 (2009). URL <https://link.aps.org/doi/10.1103/PhysRevB.79.054528>.
- [15] He, R. H. *et al.* Superconducting order parameter in heavily overdoped $\text{Bi}_2\text{Sr}_2\text{CaCu}_2\text{O}_{8+\delta}$:

- A global quantitative analysis. *Phys. Rev. B* **69**, 220502 (2004). URL <https://link.aps.org/doi/10.1103/PhysRevB.69.220502>.
- [16] Yang, K. *et al.* Normal-state electronic structure in the heavily overdoped regime of $\text{Bi}_{1.74}\text{Pb}_{0.38}\text{Sr}_{1.88}\text{CuO}_{6+\delta}$ single-layer cuprate superconductors: An angle-resolved photoemission study. *Phys. Rev. B* **73**, 144507 (2006). URL <https://link.aps.org/doi/10.1103/PhysRevB.73.144507>.
- [17] Mahan, G. D. *Many-Particle Physics* (Springer US, 2000), 3rd edn. URL <https://www.springer.com/gp/book/9780306463389#aboutBook>.
- [18] Wen, C. H. P. *et al.* Unveiling the superconducting mechanism of $\text{Ba}_{0.51}\text{K}_{0.49}\text{BiO}_3$. *Phys. Rev. Lett.* **121**, 117002 (2018). URL <https://link.aps.org/doi/10.1103/PhysRevLett.121.117002>.
- [19] Schäfer, J. *et al.* Electronic quasiparticle renormalization on the spin wave energy scale. *Phys. Rev. Lett.* **92**, 097205 (2004). URL <https://link.aps.org/doi/10.1103/PhysRevLett.92.097205>.
- [20] Hofmann, A. *et al.* Renormalization of bulk magnetic electron states at high binding energies. *Phys. Rev. Lett.* **102**, 187204 (2009). URL <https://link.aps.org/doi/10.1103/PhysRevLett.102.187204>.
- [21] Cui, X. *et al.* Angle-resolved photoemission spectroscopy study of Fe(110) single crystal: Many-body interactions between quasi-particles at the fermi level. *Surface Science* **601**, 4010 – 4012 (2007). URL <http://www.sciencedirect.com/science/article/pii/S0039602807003354>. ECOS-24.
- [22] Młyńczak, E. *et al.* Kink far below the fermi level reveals new electron-magnon scattering channel in Fe. *Nature Communications* **10**, 505 (2019). URL <https://doi.org/10.1038/s41467-019-08445-1>.
- [23] Rotter, M., Tegel, M. & Johrendt, D. Superconductivity at 38 k in the iron arsenide $(\text{Ba}_{1-x}\text{K}_x)\text{Fe}_2\text{As}_2$. *Phys. Rev. Lett.* **101**, 107006 (2008). URL <https://link.aps.org/doi/10.1103/PhysRevLett.101.107006>.
- [24] Pandey, A. *et al.* $\text{Ba}_{1-x}\text{K}_x\text{Mn}_2\text{As}_2$: An antiferromagnetic local-moment metal. *Phys. Rev. Lett.* **108**, 087005 (2012). URL <https://link.aps.org/doi/10.1103/PhysRevLett.108.087005>.
- [25] Bao, J.-K. *et al.* Weakly ferromagnetic metallic state in heavily doped $\text{Ba}_{1-x}\text{K}_x\text{Mn}_2\text{As}_2$. *Phys. Rev. B* **85**, 144523 (2012). URL <https://link.aps.org/doi/10.1103/PhysRevB.85.144523>.
- [26] Ramazanoglu, M. *et al.* Robust antiferromagnetic spin waves across the metal-insulator transition in hole-doped BaMn_2As_2 . *Phys. Rev. B* **95**, 224401 (2017). URL

- <https://link.aps.org/doi/10.1103/PhysRevB.95.224401>.
- [27] Zhang, W.-L. *et al.* Angle-resolved photoemission observation of mn-pnictide hybridization and negligible band structure renormalization in BaMn_2As_2 and BaMn_2Sb_2 . *Phys. Rev. B* **94**, 155155 (2016). URL <https://link.aps.org/doi/10.1103/PhysRevB.94.155155>.
- [28] Ueland, B. G. *et al.* Itinerant ferromagnetism in the as 4p conduction band of $\text{Ba}_{0.6}\text{K}_{0.4}\text{Mn}_2\text{As}_2$ identified by X-ray magnetic circular dichroism. *Phys. Rev. Lett.* **114**, 217001 (2015). URL <https://link.aps.org/doi/10.1103/PhysRevLett.114.217001>.
- [29] Singh, Y. *et al.* Magnetic order in BaMn_2As_2 from neutron diffraction measurements. *Phys. Rev. B* **80**, 100403 (2009). URL <https://link.aps.org/doi/10.1103/PhysRevB.80.100403>.
- [30] Lamsal, J. *et al.* Persistence of local-moment antiferromagnetic order in $\text{Ba}_{1-x}\text{K}_x\text{Mn}_2\text{As}_2$. *Phys. Rev. B* **87**, 144418 (2013). URL <https://link.aps.org/doi/10.1103/PhysRevB.87.144418>.
- [31] Pandey, A. *et al.* Coexistence of half-metallic itinerant ferromagnetism with local-moment antiferromagnetism in $\text{Ba}_{0.60}\text{K}_{0.40}\text{Mn}_2\text{As}_2$. *Phys. Rev. Lett.* **111**, 047001 (2013). URL <https://link.aps.org/doi/10.1103/PhysRevLett.111.047001>.
- [32] Shan, L. *et al.* Observation of ordered vortices with andreev bound states in $\text{Ba}_{0.6}\text{K}_{0.4}\text{Fe}_2\text{As}_2$. *Nature Physics* **7**, 325–331 (2011). URL <https://doi.org/10.1038/nphys1908>.
- [33] Zhang, Y. *et al.* Out-of-plane momentum and symmetry-dependent energy gap of the pnictide $\text{Ba}_{0.6}\text{K}_{0.4}\text{Fe}_2\text{As}_2$ superconductor revealed by angle-resolved photoemission spectroscopy. *Phys. Rev. Lett.* **105**, 117003 (2010). URL <https://link.aps.org/doi/10.1103/PhysRevLett.105.117003>.
- [34] Shi, J. *et al.* Direct extraction of the eliasberg function for electron-phonon coupling: A case study of $\text{Be}(\overline{10}0)$. *Phys. Rev. Lett.* **92**, 186401 (2004). URL <https://link.aps.org/doi/10.1103/PhysRevLett.92.186401>.
- [35] Kordyuk, A. A. *et al.* Bare electron dispersion from experiment: Self-consistent self-energy analysis of photoemission data. *Phys. Rev. B* **71**, 214513 (2005). URL <https://link.aps.org/doi/10.1103/PhysRevB.71.214513>.
- [36] Lanzara, A. *et al.* Evidence for ubiquitous strong electron–phonon coupling in high-temperature superconductors. *Nature* **412**, 510–514 (2001). URL <https://doi.org/10.1038/35087518>.
- [37] Horiba, K. *et al.* Isotropic kink and quasiparticle excitations in the three-dimensional perovskite manganite $\text{La}_{0.6}\text{Sr}_{0.4}\text{MnO}_3$. *Phys. Rev. Lett.* **116**, 076401 (2016). URL <https://link.aps.org/doi/10.1103/PhysRevLett.116.076401>.

- [38] Sun, Z. *et al.* Quasiparticlelike peaks, kinks, and electron-phonon coupling at the $(\pi, 0)$ regions in the cmr oxide $\text{La}_{2-2x}\text{Sr}_{1+2x}\text{Mn}_2\text{O}_7$. *Phys. Rev. Lett.* **97**, 056401 (2006). URL <https://link.aps.org/doi/10.1103/PhysRevLett.97.056401>.
- [39] Cui, X. *et al.* High-resolution angle-resolved photoemission study of Fe (110). *Physica B: Condensed Matter* **383**, 146 – 147 (2006). URL <http://www.sciencedirect.com/science/article/pii/S0921452606007745>.
- [40] Hayashi, H. *et al.* High-resolution angle-resolved photoemission study of electronic structure and electron self-energy in palladium. *Phys. Rev. B* **87**, 035140 (2013). URL <https://link.aps.org/doi/10.1103/PhysRevB.87.035140>.
- [41] Wray, L. *et al.* Momentum dependence of superconducting gap, strong-coupling dispersion kink, and tightly bound cooper pairs in the high- T_c $(\text{Sr}, \text{Ba})_{1-x}(\text{K}, \text{Na})_x\text{Fe}_2\text{As}_2$ superconductors. *Phys. Rev. B* **78**, 184508 (2008). URL <https://link.aps.org/doi/10.1103/PhysRevB.78.184508>.
- [42] Kresse, G. & Furthmüller, J. Efficiency of ab-initio total energy calculations for metals and semiconductors using a plane-wave basis set. *Computational Materials Science* **6**, 15 – 50 (1996). URL <http://www.sciencedirect.com/science/article/pii/S0927025696000080>.
- [43] Kresse, G. & Furthmüller, J. Efficient iterative schemes for ab initio total-energy calculations using a plane-wave basis set. *Phys. Rev. B* **54**, 11169 (1996). URL <https://link.aps.org/doi/10.1103/PhysRevB.54.11169>.
- [44] Togo, A. & Tanaka, I. First principles phonon calculations in materials science. *Scripta Materialia* **108**, 1 – 5 (2015). URL <http://www.sciencedirect.com/science/article/pii/S1359646215003127>.
- [45] Perdew, J. P., Burke, K. & Ernzerhof, M. Generalized gradient approximation made simple. *Phys. Rev. Lett.* **77**, 3865–3868 (1996). URL <https://link.aps.org/doi/10.1103/PhysRevLett.77.3865>.
- [46] Toth, S. & Lake, B. Linear spin wave theory for single-q incommensurate magnetic structures. *Journal of Physics: Condensed Matter* **27**, 166002 (2015). URL <https://doi.org/10.1088/0953-8984/27/16/166002>.
- [47] Glasbrenner, J. K. & Mazin, I. I. First-principles evidence of mn moment canting in hole-doped $\text{Ba}_{1-2x}\text{K}_{2x}\text{Mn}_2\text{As}_2$. *Phys. Rev. B* **89**, 060403 (2014). URL <https://link.aps.org/doi/10.1103/PhysRevB.89.060403>.
- [48] Takahashi, T. *et al.* Para- to ferromagnetic phase transition of CoS_2 studied by

- high-resolution photoemission spectroscopy. *Phys. Rev. B* **63**, 094415 (2001). URL <https://link.aps.org/doi/10.1103/PhysRevB.63.094415>.
- [49] Okabayashi, J. *et al.* Ferromagnetic transition in MnP studied by high-resolution photoemission spectroscopy. *Phys. Rev. B* **69**, 132411 (2004). URL <https://link.aps.org/doi/10.1103/PhysRevB.69.132411>.
- [50] Zhang, Y. *et al.* Emergence of kondo lattice behavior in a van der waals itinerant ferromagnet Fe₃GeTe₂. *Science Advances* **4**, eaao6791 (2018). URL <https://advances.sciencemag.org/content/4/1/eaao6791>. <https://advances.sciencemag.org/content/4/1/eaao6791.full.pdf>.
- [51] Capellmann, H. Theory of itinerant ferromagnetism in the 3-d transition metals. *Zeitschrift für Physik B Condensed Matter* **34**, 29–35 (1979). URL <https://doi.org/10.1007/BF01362776>.
- [52] Fazekas, P. *Lecture notes on electron correlation and magnetism*, vol. 5 (World scientific, 1999).
- [53] Creveling, L., Luo, H. L. & Knapp, G. S. Ferromagnetism in Au₄V. *Phys. Rev. Lett.* **18**, 851–852 (1967). URL <https://link.aps.org/doi/10.1103/PhysRevLett.18.851>.
- [54] Adachi, K., Matsui, M. & Fukuda, Y. Magnetic properties of au₄v single crystal. *Journal of the Physical Society of Japan* **48**, 62–70 (1980). URL <https://doi.org/10.1143/JPSJ.48.62>. <https://doi.org/10.1143/JPSJ.48.62>.
- [55] An, J., Sefat, A. S., Singh, D. J. & Du, M.-H. Electronic structure and magnetism in BaMn₂As₂ and BaMn₂Sb₂. *Phys. Rev. B* **79**, 075120 (2009). URL <https://link.aps.org/doi/10.1103/PhysRevB.79.075120>.
- [56] Strocov, V. *et al.* Soft-X-ray ARPES facility at the adress beamline of the sls: Concepts, technical realisation and scientific applications. *Journal of synchrotron radiation* **21**, 32–44 (2014). URL <https://doi.org/10.1107/S1600577513019085>.

We gratefully acknowledge the experimental support of Dr. Y. B. Huang, Dr. Z. Sun, Dr Z. T. Liu, and Dr. D. W. Shen. We thank the Diamond Light Source for time on beam line I05, the Advanced Light Source (U.S. DOE contract no. DE-AC02-05CH11231) for access to beamline 4.0.3, the Stanford Synchrotron Radiation Light Source for the access to beamline 5-2, and the Swiss Light Source for time on SX-ARPES endstation of beamline ADDRESS. Some preliminary data were taken at National Synchrotron Radiation Laboratory (NSRL, China) and BL03U at Shanghai Synchrotron Radiation Facility. This work is supported in part by the National Natural Science Foundation of China (Grants No. 11888101, 12074074, 11704074, 11704073, and 11790312),

the National Key R&D Program of the MOST of China (Grants No. 2016YFA0300200 and 2017YFA0303004), Project supported by Shanghai Municipal Science and Technology Major Project (Grant No. 2019SHZDZX01), and Shanghai Rising-Star Program (20QA1401400).

[Competing Interests] The authors declare that they have no competing financial interests.

[Correspondence] Correspondence and requests for materials should be addressed to H.C.X. (email: xuhaichao@fudan.edu.cn) and D.L.F. (email: dlheng@fudan.edu.cn).

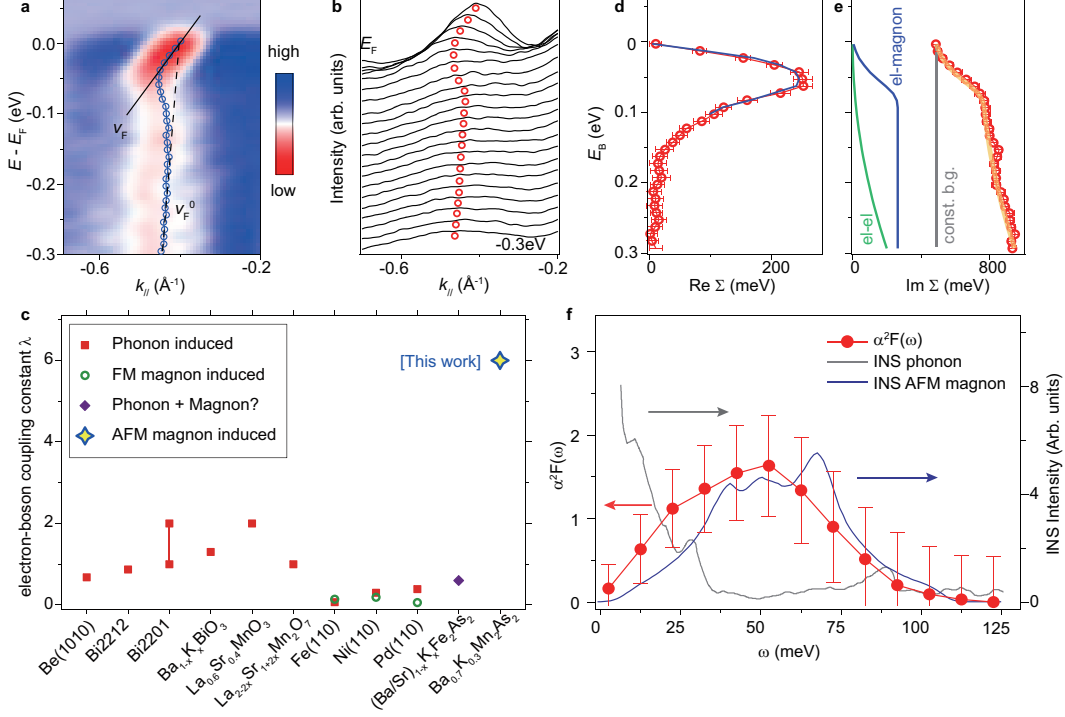


FIG. 2: **Kink and self-energy analysis showing the electron-magnon interaction for $\text{Ba}_{0.7}\text{K}_{0.3}\text{Mn}_2\text{As}_2$.**

(a) Second derivative spectra of the enlargement near the Fermi crossing of the α band (rectangular area in Fig. 1g), overlaid with the fitting of the Fermi velocity v_F (solid line) and the bare band velocity v_F^0 (dashed line). (b) Momentum distribution curves (MDCs) of photoemission intensity around the Fermi crossing of the α band. The circles track the MDC peaks and illustrate the band dispersion. (c) The reported electron-boson coupling constant obtained based on MDC analysis of kinks in ARPES data of Be(1010) [34], Bi2212 [35], Bi2201 [36], $\text{Ba}_{1-x}\text{K}_x\text{BiO}_3$ [18], $\text{La}_{0.6}\text{Sr}_{0.4}\text{MnO}_3$ [37], $\text{La}_{2-2x}\text{Sr}_{1+2x}\text{Mn}_2\text{O}_7$ [38], Fe(110) [21, 39], Ni(110) [20], Pd(110) [40], and $(\text{Ba}/\text{Sr})_{1-x}\text{K}_x\text{Fe}_2\text{As}_2$ [41], together with that of $\text{Ba}_{0.7}\text{K}_{0.3}\text{Mn}_2\text{As}_2$. (d) $\text{Re } \Sigma$ (red) and the KK transformation of $\text{Im } \Sigma$ below 115 meV (blue curve). (e) The KK transformation of $\text{Re } \Sigma$ (blue curve), the electron-electron scattering (green curve), and a constant background (grey curve). The orange curve shows their combination, which matches well with $\text{Im } \Sigma$ (red circles). (f) Eliashberg function (red) extracted from the $\text{Im } \Sigma$, compared with the phonon (purple) and magnon (blue circles) intensity from inelastic neutron scattering (INS) and simulated magnetic intensity (blue curve) on $\text{Ba}_{1-x}\text{K}_x\text{Mn}_2\text{As}_2$ ($x=0.25$) (ref. 26).

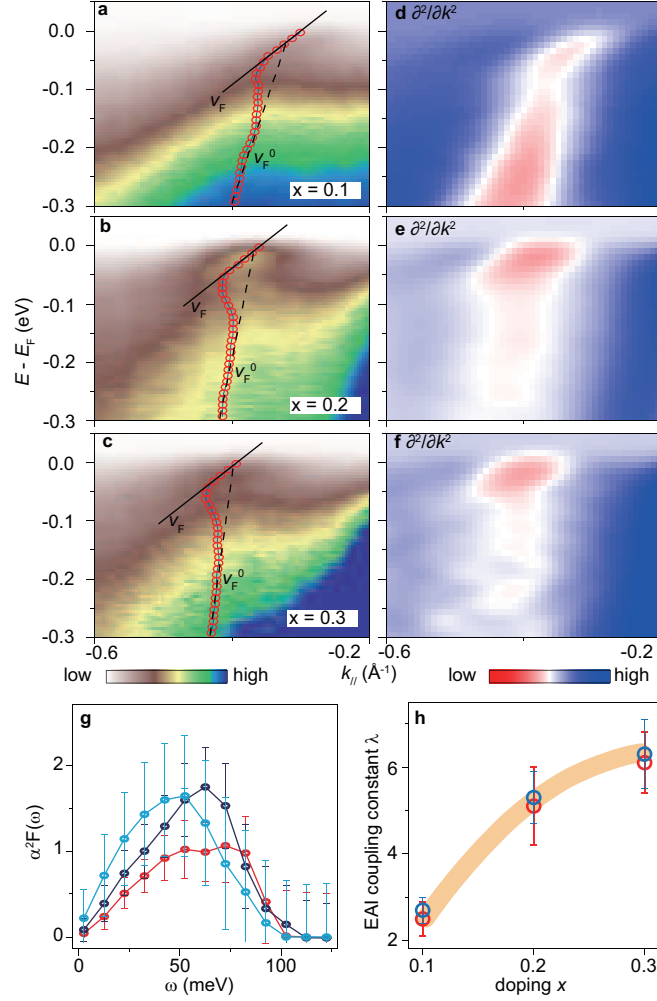


FIG. 3: Doping dependence of electron-magnon interactions. (a-c) Photoemission intensity near the Fermi crossing of the α band along ΓX , measured with 78 eV photons at 30 K for samples of $x = 0.1$, 0.2 and 0.3, respectively. The overlaid dispersion is obtained by fitting the MDCs. The solid lines and dashed lines illustrate the Fermi velocity and the bare band velocity, respectively. (d-f) Corresponding second derivative of panels (a-c). (g) Eliashberg function $\alpha^2 F(\omega)$ for samples of different dopings. (h) Evolution of the coupling constant as a function of the doping calculated through the band velocity renormalization (red) and $\text{Im } \Sigma$ (blue).

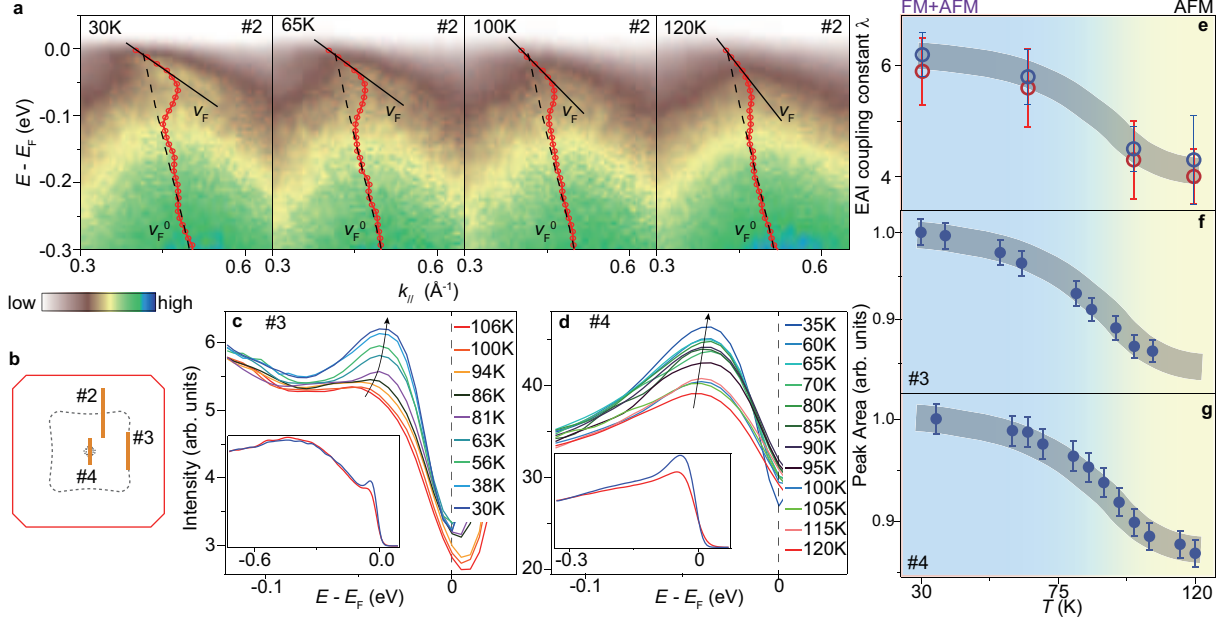


FIG. 4: Evolution of Electron-magnon interaction as a function of the temperature. (a) Photoemission intensity along momentum cut #2 of $\text{Ba}_{1-x}\text{K}_x\text{Mn}_2\text{As}_2$ ($x = 0.3$) at temperatures of 30 K, 65 K, 100 K and 120 K, overlaid with the band dispersion determined by the MDC peaks (red circles). The solid lines and dashed lines illustrate the Fermi velocity and the bare band velocity, respectively. (b) Sketch of the Fermi surface and momenta of photoemission cuts. (c-d) Photoemission spectra of different temperatures integrated along cut #3 and cut #4 in panel b, respectively. The spectra are divided by a resolution-convolved Fermi-Dirac function to remove the thermal effect near E_F . The insets show integrated spectra at a larger energy window. (e) Coupling constant as a function of the temperature. The results are obtained by band velocity renormalization (red) and $\text{Im } \Sigma$ (blue). (f-g) Quasiparticle peak intensity integrated over $[E_F - 0.08 \text{ eV}, E_F + 0.05 \text{ eV}]$ as a function of the temperature for the spectra in panels c and d, respectively. The colour background illustrates the transition between the AFM phase and FM-AFM coexisting phase. The spectra were measured with 78 eV photons.

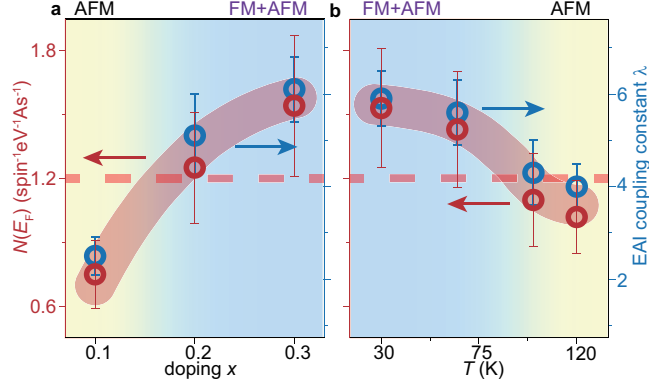


FIG. 5: **Density of states and coupling constant in the temperature-doping phase diagram.** (a) Electronic density of states ($N(E_F)$, red circles) and EAIs coupling constant (λ , blue circles) as a function of the doping at 30 K. (b) Same as (a) but as a function of the temperature for $x=0.3$. The colour background illustrates the transition between the AFM phase and FM-AFM coexisting phase. The horizontal dashed line illustrates the Stoner criteria assuming $I_{As} \sim 0.8$ eV, to fit the phase boundary of the ferromagnetic phase.